PCCP
Physical Chemistry Chemical Physics

Accepted Manuscript

This article can be cited before page numbers have been issued, to do this please use: S. Moxon, A. Symington, J. S. Tse, J. Dawson, J. Flitcroft, S. Parker, D. J. Cooke, R. M. Harker and M. Molinari, *Phys. Chem. Chem. Phys.*, 2020, DOI: 10.1039/D0CP00021C.

ROYAL SOCIETY OF CHEMISTRY

rsc.li/pccp

View Article Online
DOI: 10.1039/D0CP00021C

ARTICLE

The Energetics of Carbonated PuO_2 Surfaces Affects Nanoparticle Morphology: A DFT+U Study

Received 00th January 20xx,
Accepted 00th January 20xx

DOI: 10.1039/x0xx00000x

Samuel Moxon,[a] Adam R. Symington,[b] Joshua S. Tse,[a] James Dawson,[a] Joseph M. Flitcroft,[a] Stephen C. Parker,[b] David J. Cooke,[a] Robert M. Harker,[c] and Marco Molinari*[a]

Radiolytic corrosion of actinide materials represent an issue for the long term storage and disposal of nuclear materials. Molecular species adsorbed at the surface of the actinides may impact the rate of radiolysis, and as the surfaces corrode, the soluble toxic and radioactive species leach into groundwater. It is therefore critical to charcterise the surface composition of actinides. Here, we employ *ab initio* modelling to determine the surface composition of PuO_2 with respect to adsorbed CO_2. We found that CO_2 interacts strongly to the surface forming carbonate species. By mapping the energetics of this interaction, we then calculate the temperature of desorption, finding that surface morphology has a strong impact on the adsorption of CO_2, with the {100} being the most and the {111} the least affected by carbonation. Finally, we predict the effect of carbonation on the morphology of PuO_2 nanoparticles as a function of temperature and pressure, finding that a truncated octahedral is the preferred morphology. This modelling strategy helps characterise surface compensition and nanoparticle morphology, and we discuss the implication for radiolytically driven dispersal of material into the environment.

Introduction

Plutonium dioxide, PuO_2, enters the nuclear cycle as a by-product from reprocessing of spent nuclear fuel.[1] Plutonium (Pu) is a long-lived toxic radionuclide[2] and requires dedicated facilities[3] to handle. Despite this, the UK has not yet fully developed a comprehensive strategy for its ~100 tonne inventory of Pu stored as PuO_2,[1] which is around 20% of the world's total Pu reserves.[4,5] The inability to safely treat and store Pu and other actinides is a significant and challenging technological and environmental issue, due to concerns over its toxicity and radioactivity. [5]

PuO_2 samples have a relatively high surface area and as such large quantities of contaminants are able to adsorb.[6] Surface speciation and surface chemistry are therefore important aspects in the broader context of radiolytic corrosion of the material during long-term storage and reprocessing.[7] Radiolysis can lead to surface actinide species leaching into the environment.[5] Radiolysis of groundwater close to the nuclear material produces reactive oxygen species (*e.g.* hydrogen peroxide, H_2O_2, and hydroxyl radicals) that go on to react with the actinide surface.[8] Species adsorbed at the surface can therefore regulate, under some circumstances, the rate of radiolytically driven dispersal of material into the environment. Carbon dioxide (CO_2) is such a species, with claims that adsorbed CO_2 can increase[9–12] or decrease[13,14] the rate of environmental dispersal in the case of UO_2. Although the mechanism and kinetics of this dispersal is complex, the role of dissolved CO_2 in reacting with hydroxyl radicals is recognised.[12,15] Independent of this, key questions remain on the role of surface bound CO_2 on environmental dispersal. Currently there is very little information on the interaction of CO_2 and PuO_2, either from modelling[16] or experiments.[6,17–19]

The inherent radioactivity and availability of actinide materials make them attractive to study computationally. While *ab initio* molecular modelling remains relatively in its infancy to model surface radiolytic processes directly, there are computational strategies that can provide insights on surface composition and morphology. This is not without its limitations, as the *ab initio* modelling needs to describe the heavy-fermion systems reliably and accurately, which means that exchange-correlation, relativistic contributions, spin-orbit interactions and noncollinear magnetism add to the complexity of the problem.[20–23]

Here, we present a comprehensive modelling study on the interaction of CO_2 with surfaces of PuO_2, which we couple with a thermodynamic strategy to link molecular level insights to phase diagrams to map the stability of PuO_2 surfaces and the morphology of PuO_2 nanoparticles under varying temperature and pressure conditions. Finally, we discuss the implications within the context of radiolysis.

Computational Methodology

We use density functional theory (DFT) calculations as coded within the Vienna Ab-initio Simulation Package (VASP)

[a] Department of Chemical Sciences, University of Huddersfield, Queensgate, Huddersfield, HD1 3DH, UK. Corresponding author: m.molinari@hud.ac.uk
[b] Department of Chemistry, University of Bath, Claverton Down, Bath, BA2 7AY, UK.
[c] AWE Aldermaston, Reading, RG7 4PR, UK

Electronic Supplementary Information (ESI) available: Section S1: Structure and magnetisation of bulk structures. Section S2: Structure and magnetisation of bare surfaces. Section S3: Structural Configurations. Section S4: Structure and magnetisation of {100}. Section S5: Structure and magnetisation of {110}. Section S6: Structure and magnetisation of {111}. See DOI: 10.1039/x0xx00000x

software.[24] Our simulations used a plane-wave basis set, which incorporates relativistic effect core potentials and the projector augmented wave (PAW) method.[25,26] The cut-off energy of the plane-wave basis set was 500 eV as Pegg *et al*.[21,23] The frozen core is [Xe] for Pu and [He] for C and O. The exchange-correlation functional applied was the Perdew-Burke-Ernzerhof for solids (PBEsol).[27]

When considering highly correlated *f*-electron systems, such as PuO_2, difficulties arise due to the hybridisation of the 5*f* wave function with 6*d* or 7*s* bands, or the overlapping of 5*f* wave functions of adjacent Pu atoms.[28] Standard DFT incorrectly captures the electronic structure of PuO_2 to be a ferromagnetic (FM) conductor,[29] as opposed to the antiferromagnetic (AFM) Mott insulator.[30] To overcome this, we include the Hubbard U correction,[31] using the Liechtenstein[32] methodology, where the coulombic (U) and exchange (J) parameters are treated as independent variables. We chose U = 6 eV and J = 0 eV; this choice makes the Liechtenstein and the Dudarev[33] methods equivalent. Previous work by Pegg *et al*. has evaluated the effect of changing the Hubbard U parameter on physical properties of PuO_2, concluding that the U_{eff} = 6 eV performs best overall.[21] All calculations consider spin-orbit interactions (SOI)[34] and noncollinear magnetic wave vectors.

Bulk PuO_2

The bulk structure was minimised using the conjugate gradient with electronic and ionic iteration thresholds of $1x10^{-5}$ eV/atom and $1x10^{-3}$ eV $Å^{-1}$. The Brillouin zone was sampled using a Γ-centred 5 x 5 x 5 k-point grid. A longitudinal 3K AFM model using noncollinear magnetic wave-vectors and SOI[34] were used to describe the complex electronic and magnetic structures. The magnetisation is represented in Figure 1. The minimised bulk full unit cell (4 PuO_2 units) resulted in a $Fm\bar{3}m$ (No. 225) crystal symmetry with a lattice constant of 5.417Å (expt value 5.396-5.398 Å),[35–38] and a total magnetisation per Pu atom of 3.80 μ_B, characteristic of Pu^{4+}.[21] Further details are provided in Supporting Information (SI) (section S1).

Bulk Pu_2O_3

The bulk structure of Pu_2O_3 was minimised with the same settings as bulk PuO_2 including the use of SOI, but the Brillouin zone was sampled using a Γ-centred 4 x 4 x 4 k-point grid, which was deemed to be converged. The initial magnetisation was the longitudinal 3K AFM as for the PuO_2. Further details are in the SI (section S1). The minimised bulk full unit cell resulted in an Ia-3 (No. 206) crystal symmetry with a lattice constant of 11.09 Å (expt value 10.98 Å),[39] and a total magnetisation per Pu atom of 4.81 μ_B, indicative of Pu^{3+}.

PuO_2 Surfaces

Figure 1 shows the Miller indices of the {100}, {110} and {111} surfaces under investigation mapped onto the bulk unit cell. The surfaces of PuO_2 were generated from the minimised bulk full unit cell using the METADISE code[40]. The unit cell was rotated

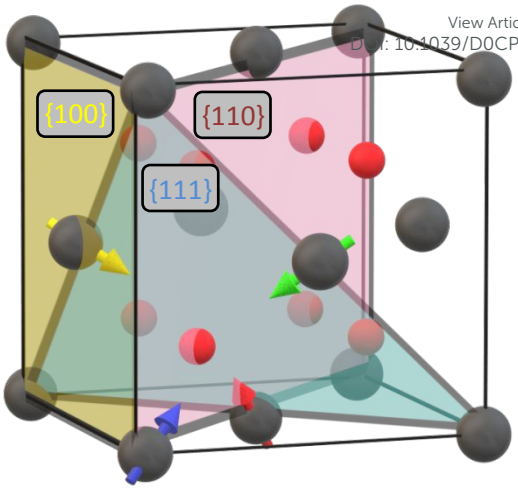

Figure 1 - The bulk unit cell of PuO_2. Pu atoms in grey and O atoms in red. The arrows dictate the direction of the magnetic vector for Pu atoms. The yellow, red and blue planes represent the surfaces with {100}, {110} and {111} Miller indices.

so the Miller index of choice is perpendicular to the *x* axis and cuts are made to expose surfaces. The removal of the dipole perpendicular to the {100} surface occurred by transposing half the oxygen atoms on the top surface onto the bottom one; we chose the most stable arrangement according to the literature.[23] By then ensuring that the termination of the surfaces are mirror planes, this allows the use of the slab method, where all the atoms in the slabs are allowed to relax and the top and bottom surfaces are symmetric. The {100}, {110} and {111} surfaces are ($\sqrt{2}$ x $\sqrt{2}$), (2 x $\sqrt{2}$), and (1 x 1) expansions of the full unit cell with 7 (28 PuO_2 units), 7 (28 PuO_2 units), and 5 (20 PuO_2 units) Pu atomic layers respectively. A minimum of 15 Å vacuum gap was introduced to isolate periodic image interaction. The thickness of the slabs and the number of atomic layers are converged with respect to surface energy according to Pegg *et al*.[23] The structures of the slabs are presented in the SI (section S2). Our oxygen-deficient (abbreviated as O-deficient) slabs were generated from the stoichiometric slab by introducing an oxygen vacancy symmetrically on the top and bottom surfaces of the slab configuration; this introduces two excess electrons that localise on Pu sites so that two Pu^{4+} reduce to two Pu^{3+}. We have not placed any constraints on the localisation of the excess electrons. The slabs of PuO_2 were minimised including the use of SOI and using the conjugant gradient method with an electronic and an ionic convergence criteria of $1x10^{-5}$ eV/atom and $1x10^{-2}$ eV $Å^{-1}$/atom respectively. The Brillouin zone was sampled using a 2 x 2 x 1 k-point grid, which was deemed to be converged; selected calculations were performed with the 4 x 4 x 1 k-point grid[23] but no energy change was observed. When realigning the magnetic vectors, the spin quantisation axis was orientated in the direction perpendicular to the surface.

Molecules

Isolated O_2 and CO_2 molecules were simulated at the Γ point using a 10 $Å^3$ cubic cell to avoid image interaction and the same ionic and electronic convergence criteria as the surface calculations.

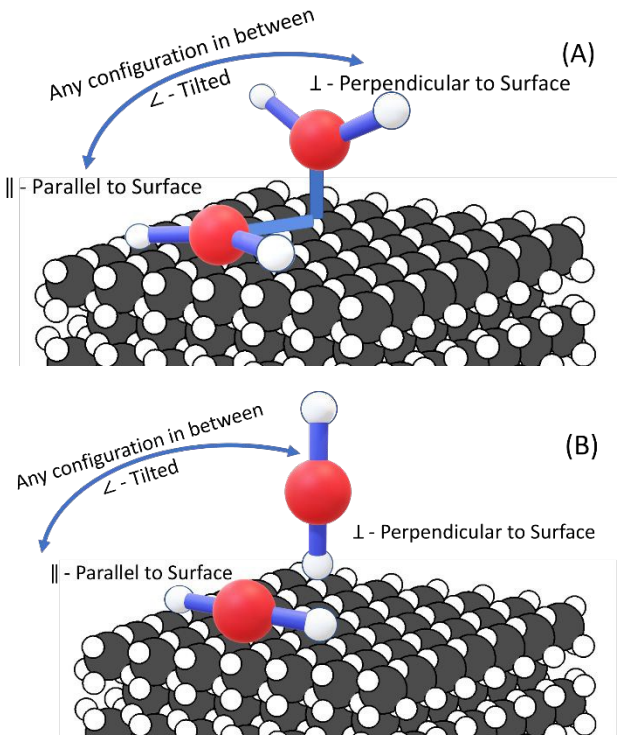

Figure 2 - Representation of the associative (A) and molecular (B) adsorption of CO_2 on the surface of PuO_2

Surface CO_2 Adsorption

The adsorption of CO_2 on the {100}, {110} and {111} surfaces was considered for different starting configurations to sample the structural (and energy) landscape of the adsorption. The adsorbed CO_2 at the top and bottom of the slab were symmetrically equivalent. Our model surfaces do not consider co-adsorption of CO_2 and water, adsorbed at the surfaces of PuO_2 either in molecular of distinctive form, in this study. Figure 2 depicts the adsorbed CO_2: we refer to "associative adsorption" (Figure 2A) as a CO_2 molecule forming an adsorbed carbonate species at the surface, whereas "molecular adsorption" (Figure 2B) as a CO_2 molecule remains above the surface. From all the starting configurations trialled, only a finite number remained stable after geometry optimization; details of all trials are presented in the SI (section S4-S6). No vibrational analysis has been performed in this work, although this should be the focus for future work as it provides additional information on the strength of the CO_2 adsorption.

Surface Energetics

The surface energy ($\gamma_{(\mathrm{Stoich})}$) of the stoichiometric surfaces was calculated as

$$\gamma_{(\mathrm{Stoich})} = \frac{E_{\mathrm{Slab}}^{\mathrm{Stoich}} - E_{\mathrm{Bulk,PuO_2}}}{2A} \qquad (1)$$

and the surface energy ($\gamma_{(Redu)}$) of oxygen-deficient surfaces as

$$\gamma_{(\mathrm{Redu})} = \frac{E_{\mathrm{Slab}}^{\mathrm{Redu}} - \left(E_{\mathrm{Bulk,PuO_2}} + E_{\mathrm{Bulk,Pu_2O_3}}\right)}{2A} \qquad (2)$$

where $E_{\mathrm{Slab}}^{\mathrm{Stoich}}$ and, $E_{\mathrm{Slab}}^{\mathrm{Redu}}$ are the energies of the stoichiometric and oxygen-deficient slabs, E_{Bulk} is the energy of bulk PuO_2 and Pu_2O_3 chosen to maintain the same number of Pu and O species in the slab configurations, A is the surface area of one face of the slab and the factor 2 occurs as the slab configurations express two identical surfaces.

The heat of reduction was calculated as

$$E_{\mathrm{Redu}} = \frac{E_{\mathrm{Slab}}^{\mathrm{Redu}} + E_{O_2} - E_{\mathrm{Slab}}^{\mathrm{Stoich}}}{2} \qquad (3)$$

where E_{O_2} is the energy of an oxygen molecule; dividing by two accounts for an oxygen vacancy on both sides of the slab.

The energy of adsorption of CO_2 on stoichiometric surfaces was calculated as

$$E_{\mathrm{Ads}}^{\mathrm{Stoich}} = \frac{E_{\mathrm{Slab}}^{\mathrm{Stoich,Ads}} - \left(E_{\mathrm{Slab}}^{\mathrm{Stoich}} + nE_{\mathrm{CO_2}}\right)}{n} \qquad (4)$$

and on the oxygen-deficient surfaces:

$$E_{\mathrm{Ads}}^{\mathrm{Redu}} = \frac{E_{\mathrm{Slab}}^{\mathrm{Redu,Ads}} - \left(E_{\mathrm{Slab}}^{\mathrm{Redu}} + nE_{\mathrm{CO_2}}\right)}{n} \qquad (5)$$

where $E_{\mathrm{Slab}}^{\mathrm{Stoich,Ads}}$ and $E_{\mathrm{Slab}}^{\mathrm{Redu,Ads}}$ are the energies of the stoichiometric and oxygen-deficient slabs with CO_2 adsorbed on the surface; dividing by n accounts for the CO_2 adsorption on both sides of the slab (this work n = 2).

Phase Diagrams

Pressure and temperature effects are introduced according to the approach of Sun *et al.*[41] and implemented successfully for oxides including lanthanides and actinides[42–45] so that a surface energy for surfaces with adsorbed species, $\gamma_{(\mathrm{Ads})}$, is

$$\gamma_{(\mathrm{Ads})} = \gamma_{(\mathrm{Bare})} + \left(C\left(E_{\mathrm{Slab}}^{\mathrm{Ads},(T)} - RTln\left(\frac{p_{\mathrm{Ads}}}{p^{\circ}}\right)\right)\right) \qquad (6)$$

where $\gamma_{(\mathrm{Bare})}$ is the surface energy of the bare surface, calculated according to Equation 1 for the stoichiometric surfaces (*i.e.* $\gamma_{(\mathrm{Bare})} = \gamma_{(\mathrm{Stoich})}$) and Equation 2 for the oxygen-deficient surfaces (*i.e.* $\gamma_{(\mathrm{Bare})} = \gamma_{(\mathrm{Redu})}$), C is the coverage of the adsorbing species (*i.e.* CO_2 or O_2), and

$$E_{\mathrm{Slab}}^{\mathrm{Ads},(T)} = \frac{E_{\mathrm{Slab}}^{\mathrm{Ads}} - \left(E_{\mathrm{Bare}} + n_{\mathrm{Ads}}E_{\mathrm{Ads},(T)}\right)}{n_{\mathrm{Ads}}} \qquad (7)$$

$E_{\mathrm{Slab}}^{\mathrm{Ads},(T)}$ is the energy of the slab with the adsorbed species (*i.e.* $E_{\mathrm{Ads}} = E_{\mathrm{Slab}}^{\mathrm{Stoich,Ads}}$ for the stoichiometric surface and $E_{\mathrm{Ads}} = E_{\mathrm{Slab}}^{\mathrm{Redu,Ads}}$ for the oxygen-deficient surface), E_{Bare} is the energy of the bare surface (*i.e.* $E_{\mathrm{Bare}} = E_{\mathrm{Slab}}^{\mathrm{Stoich}}$ for stoichiometric surfaces (Equation 1) or $E_{\mathrm{Bare}} = E_{\mathrm{Slab}}^{\mathrm{Redu}}$ for oxygen-deficient surfaces (Equation 2)), n_{Ads} is the number of adsorbed molecules and

$$E_{\mathrm{Ads},(T)} = E_{\mathrm{Ads},(g)} - TS_{(T)}^{\circ} \qquad (8)$$

$E_{\mathrm{Ads},(T)}$is the energy of the adsorbate as a function of temperature, $E_{\mathrm{Ads},(g)}$ is the energy of the gaseous adsorbate (*i.e.* CO_2 and O_2), $S_{(T)}^{\circ}$ is the experimental entropy of the gaseous molecule in the standard state[46] and T is the temperature.

Based upon the surface energies calculated using Equation 6, the area of each surface expressed can be calculated. These areas were then combined to give the ratio between each surface under varying pressure and temperatures, so that morphology phase diagrams can be produced as a Wulff construction,[47] to map the morphology of PuO_2 nanoparticle as a function of pressure and temperature.

Visualisation and Imaging

VESTA[48] was used in visualisation and creation of images. The analysis was performed using the surfinpy code[49] and Wulff constructions generated using pymatgen.[50]

Results and Discussion

PuO_2 Surface Structures

The relaxed {100}, {110} and {111} surfaces are presented in Figure 3. We find that there is no significant structural relaxation at the surface of the {110} and {111} surfaces, however, the surface and subsurface oxygen layers of the {100} surface undergo large relaxation (Figure 3d). These findings have been reported previously in PuO_2[51,52] and other fluorite structures such as UO_2,[51,53] CeO_2[54] and ThO_2.[55]

PuO_2 Surface Energetics

The surface energy (Equation 1 and Equation 2) of the stoichiometric and oxygen-deficient {100}, {110} and {111} surfaces is presented in Table 1. The most stable stoichiometric surface is the {111} followed by the {110} and the {100} surfaces. This order of stability is comparable to previous DFT studies on PuO_2,[23,43,51] and other fluorite structures including UO_2,[43,51] ThO_2[56,57] and CeO_2.[42] Analogous to the stoichiometric surfaces, the surface energies for oxygen-deficient PuO_2 surfaces follow the same order of {111} < {110} < {100}. The value of the surface energy increases when the surface is oxygen-deficient compared to the stoichiometric case for the {111} and the {110}, however the opposite occurs for the {100}. Although there is not much information on oxygen-deficient surfaces of actinide oxides, Hodkin and Nicholas, using Sessile drop experiments,[58] measured values of 0.34 J m^{-2} and 0.90 J m^{-2} for the stoichiometric and oxygen-deficient {111} of UO_2, which appears to support our energy shift for PuO_2 surfaces.

The heat of reduction (Equation 3) of the three surfaces was investigated by removal of an oxygen atom, with two excess electrons that localise on Pu atoms. According to Table 1, where a lower energy values means it is easier to form an oxygen vacancy, it is easier to form an oxygen vacancy on the {100} followed by the {110} and finally the {111}. This trend compares well with periodic embedded cluster model (PEECM), but not with periodic DFT+*U* (where the {100} and {110} surfaces have very similar heat of reduction) of Wellington *et al.*[59] perhaps as the latter used the 1k AFM ordering, which is not representative of the magnetic structure of PuO_2. Although comparison between the magnitude of the energy values between the present study and the PEECM calculations is somewhat different, the two studies show qualitatively good agreement. However, the two methodologies are sufficiently different that

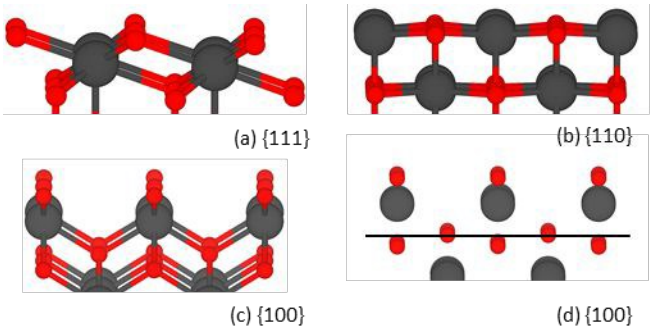

Figure 3 - The {111} (a), {110} (b) and {110} (c) surfaces of PuO_2. O atoms are red and Pu atoms are grey. (d) shows the relaxation perpendicular to the {100} surface with the black line representing the original position of the oxygen sublayer.

it is not straightforward to identify the reasons for the differences in the results. We use periodic DFT+*U* with inclusion of SOI, while the PEECM calculations have been performed with a hybrid-GGA exchange-correlation functional, and localized basis sets, with the inclusion of dispersion corrections. The periodic nature of our simulations means that the interaction of the charged defect with the surface dipole is fully incorporated. Furthermore, in contrast to our periodic DFT calculations where we have treated Pu atoms as coupled with antiferromagnetic ordering, the PEECM treats Pu atoms as coupled with ferromagnetic ordering, which is a reasonable approximation when treating a small molecular cluster of actinide oxides. It has been noted by Wellington *et al.*[59] that the local magnetic ordering appears to have little impact on the adsorption of small molecules (in their case of water molecules), which may indeed contribute to this effect. It is worth noting that a comprehensive investigation that decouples the different contributions included in the two methodologies should be performed to fully address the difference between the two.

When comparing PuO_2 with a similar fluorite structure, CeO_2, the order of the heat of reduction is different, as formation of an oxygen vacancy is easier on the {110} compared to the {100} surface.[42]

Adsorption of CO_2 on PuO_2 Surfaces

The strength of the CO_2 adsorption is dependent on its interaction with the surface, which is represented by greater negative values of energy of adsorption (Equation 4 and 5). The energies of the most stable adsorption configurations are presented in Table 2, whereas the complete set is reported in the SI (section S3). CO_2 was adsorbed on the surfaces of PuO_2 as molecular or associative species. Associative refers to CO_2 that is bonded to the surface forming a carbonate, referred to here as CO_3 (Figure 2a); the adsorption energies for associative adsorption are stronger compared to molecular adsorption (Table 2). Molecular CO_2 refers to a CO_2 molecule that is adsorbed to the surface (Figure 2b); all adsorption energies are no greater than 0.5eV.

Molecular or associative CO_2 adsorb in three main

Journal Name ARTICLE

configurations: perpendicular (⊥), parallel (∥) and tilted (∠) with respect to the surface (Figure 2).

View Article Online
DOI: 10.1039/D0CP00021C

	γ_{Stoich} / J m^{-2}		γ_{Redu} / J m^{-2}	Heat of Reduction / eV			
Surface	This Study	3k AFM DFT[23]	This Study	This study	1k AFM DFT[59]	PEECM[59]	1k AFM DFT [52]
{100}	1.98	1.96	1.90	1.99	2.50	2.29	-
{110}	1.36	1.35	1.38	2.39	2.49	2.38	1.96
{111}	0.95	0.92	1.22	3.16	3.35	3.63	2.85

Table 1 - The surface energy (J m^{-2}) of the stoichiometric and oxygen-deficient {100}, {110} and {111} PuO_2 surfaces and their corresponding heat of reduction (eV) compared to the literature.

Structure	Stoichiometric / eV			Oxygen-deficient / eV		
	{100}	{110}	{111}	{100}	{110}	{111}
CO_3 ∥	-2.69	-	-	-3.17	-	-
CO_3 ∠	-	-1.67	-0.82	-	-1.99	-1.35
CO_3 ⊥	-	-	-0.45	-1.17	-1.93	-
CO_2 ∥	-	-0.35	-	-	-0.32	-
CO_2 ∠	-	-	-0.15	-	-	-0.46
CO_2 ⊥	-	-	-	-0.43	-	-

Table 2 - Adsorption energy of CO_2 on the stoichiometric and oxygen-deficient {100}, {110} and {111} PuO_2 surfaces. Molecular and associative adsorption are referred to as CO_2 and CO_3 respectively, while ∥, ⊥ and ∠ represent configurations with the adsorbate adsorbed parallel, perpendicular or tilted with respect to the surface. A dash represents no stable configuration with that geometry was found.

Whether adsorbed molecularly or associatively, the most stable configurations were found to be parallel to the surface, followed by tilted, followed by perpendicular. This is due to an increased coordination of the surface species parallel to the surface compared to tilted and perpendicular species during the adsorption process.

Adsorption of CO_2, whether molecular or associative, is typically stronger on the oxygen-deficient surfaces compared to the adsorption on the stoichiometric surfaces, suggesting that Pu^{3+} stabilises CO_2 adsorption. The exception is molecular CO_2 adsorbed on the {110} surface, where adsorption of CO_2 is very similar for both the oxygen-deficient (-0.32 eV) and stoichiometric (-0.35 eV) surfaces.

The {100} exhibits stronger adsorption of CO_2 compared to the {110}, followed by the {111} when it comes to associatively adsorbed CO_2. The molecular adsorption of CO_2 on oxygen-deficient surfaces is predicted with a similar energy for the {111} (-0.46 eV) and the {100} (-0.43 eV), with the {110} having the least favourable adsorption (-0.32 eV).

We find that upon adsorption of CO_2 onto the {111} and {110}, there is little surface relaxation. However, this is not the case for the {100}, where the surface oxygen layer has rearranged to accommodate the adsorbed CO_2. This behaviour has been observed previously when phosphate[60] and carbonate[61] ions adsorb on the {100} of CeO_2, which is attributed to the small energy differences between the surface arrangements of oxygen species.[62] This suggests that the {100} is the most flexible and can be stabilised by manipulation of the oxygen surface layer to accommodate adsorbed species.[63,64] For CeO_2, the {100} has been observed to have a very mobile surface layer of oxygen.[65]

Adsorption processes at PuO_2 surfaces are generally studied with respect to water adsorption.[43,51,59,66–69] Surface adsorption of CO_2 on the {110} of PuO_2 has been studied by Yu *et al.,*[16] who found strongly and weakly adsorbed CO_2, governed by covalent bonding and electrostatic interactions respectively. These are structurally equivalent to our configurations; tilted associative CO_3 and the perpendicular molecular CO_2 (CO_3 ∠ and CO_2 ∥) both on the stoichiometric {110} surface. They also reported that perpendicular adsorption of CO_2 on the {110} was stable, although any of our attempts to stabilise it failed. This is likely due to Yu *et al.*[16] only using 4 Pu layers, which Pegg *et al.*[23] have shown is not sufficient to converge the surface energy. It is also unclear whether Yu *et al.*[16] include spin-orbit interaction in their calculations. Limited experimental data by early workers suggests a CO_2 physisorption (0.12 and 0.28 eV) at -80 and 30°C and at least a component of chemisorption (0.52 eV) at 90°C.[6,17] It should be noted that these are average heats of adsorption over an unknown mixture of surfaces (PuO_2 formed by decomposition of plutonium oxalate at 550°C).

Thermodynamic strategy to link the molecular to the macroscopic scale

In order to build surface phase diagrams capable of describing the interaction of CO_2 on PuO_2 surfaces as a function of temperature and CO_2 pressure, we need to consider external conditions via a thermodynamic strategy (Equation 6 to Equation 8). The next sections report the detailed results.

Reduction of PuO_2 surface - By plotting the surface energy of PuO_2 bare stoichiometric and oxygen-deficient surfaces as a function of partial pressure of O_2 and temperature (Equation 6 to Equation 8), phase diagrams mapping the reduction of PuO_2 surfaces can be drawn (Figure 4A-C). At lower temperatures the surfaces of PuO_2 are all stoichiometric, whereas high temperatures facilitate the formation of oxygen vacancies, reducing the surfaces. Figure 4D summarises the predicted temperatures required to reduce the stoichiometric surfaces, *i.e.* the lowest temperature needed at specific conditions of pressure of O_2, for the surface to become oxygen-deficient.

View Article Online
DOI: 10.1039/D0CP00021C

ARTICLE

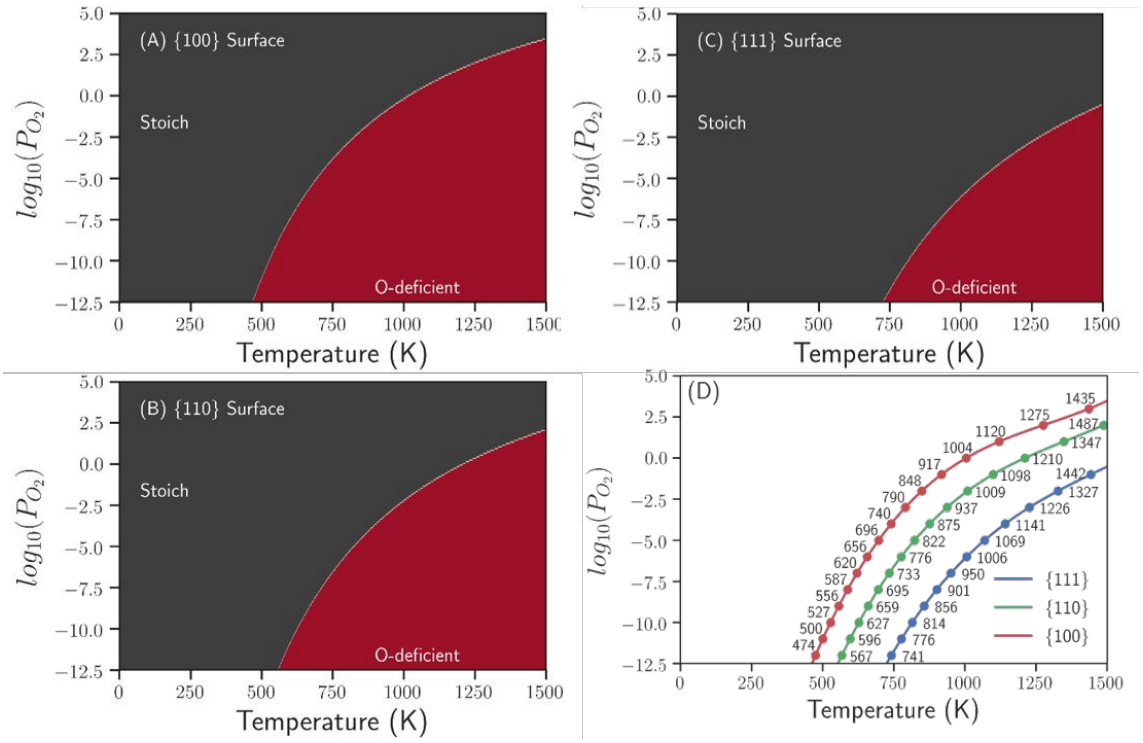

Figure 4 - Pressure of O_2 (bar) vs temperature (K) phase diagrams for the reduction of PuO_2 {100} (A), {110} (B), {111} (C). For clarity, the grey region denotes the stoichiometric surface and the red region denotes the oxygen-deficient surface. (D) Temperature of desorption of O_2 from the stoichiometric to the oxygen-deficient surface. The {111}, {110} and the {100} surfaces are shown in blue, green and red. The temperature of desorption at pressures ranging from -12.5 $\log_{10}(P(O_2))$ (bar) to 5 $\log_{10}(P(O_2))$ (bar) in increments of 1 are marked at the corresponding locations on the plots.

DOI: 10.1039/D0CP00021C

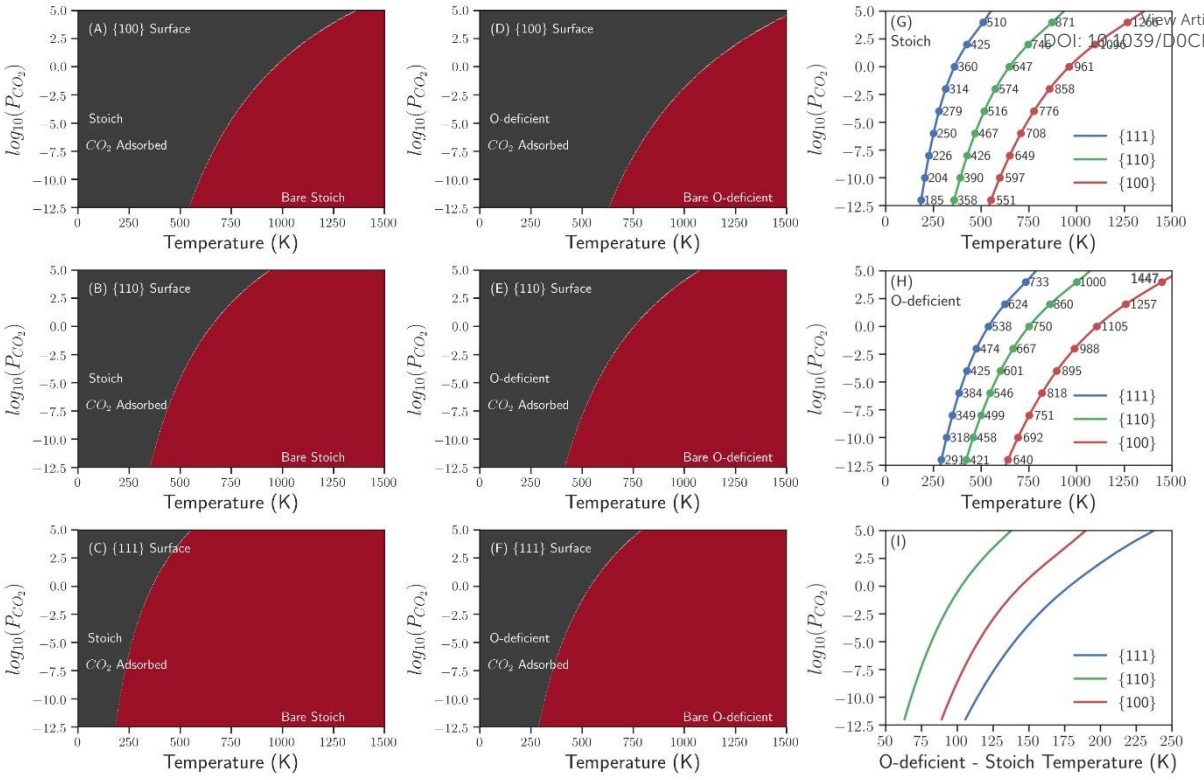

Figure 5 - Pressure of CO_2 (bar) vs Temperature (K) phase diagrams for the adsorption of CO_2 on the stoichiometric {100} (A), {110} (B), {100} (C) and the oxygen-deficient {100} (D), {110} (E) and {111} (F) surfaces. The red region no CO_2 is adsorbed while and the grey region has adsorbed CO_2. The temperature of desorption of CO_2 for the stoichiometric (G) and the oxygen-deficient (H) surfaces. The temperature of desorption at pressures ranging from -12.5 $log_{10}(P(O_2))$ (bar) to 5 $log_{10}(P(O_2))$ (bar) in increments of 1 are marked at the corresponding locations on the plots. (I) represents the difference between the stoichiometric and the oxygen-deficient case. The {111}, {110} and the {100} surfaces are shown in blue, green and red.

View Article Online
DOI: 10.1039/D0CP00021C

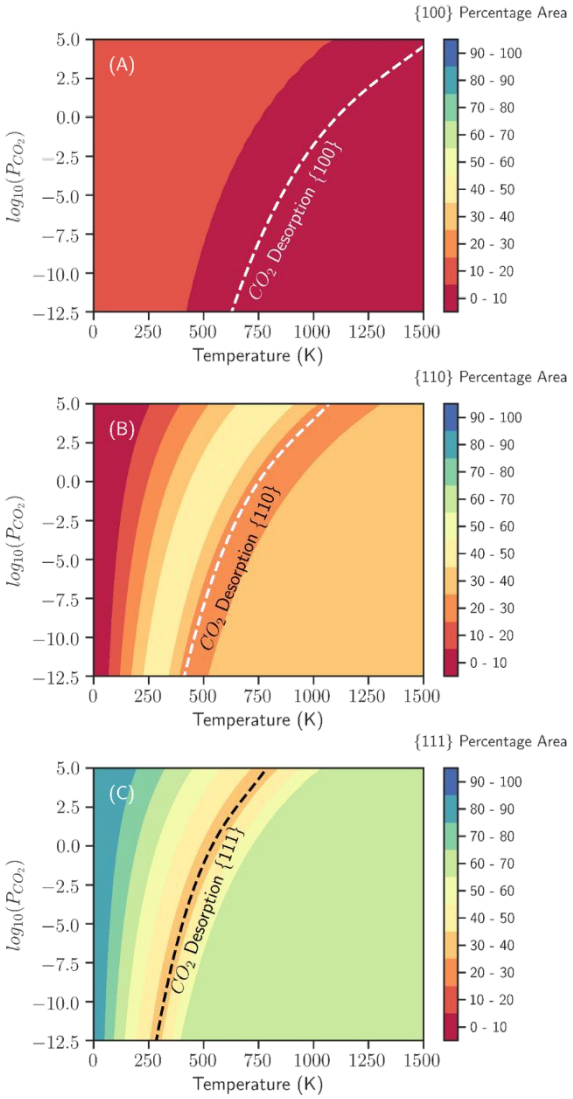

Figure 6 – Phase diagrams demonstrating the percentage surface area for the {100} (A), {110} (B), {111} (C) as a function of pressure (bar) and temperature (K). Phase diagrams refer to oxygen-deficient surfaces

According to this analysis, vacancies can be introduced on the {100} surface at temperatures as low as 475 K (202 °C) under UHV conditions (10^{-10} bar). Stakebake[18] observed O_2 as a desorption product of PuO_2 exposed to water vapour at 300 and 700 °C, although this may be related to the reaction of PuO_{2-x} with H_2O. Higher temperatures are required for the reduction of the {111}, followed by the {110} and the {100} surfaces. This follows the same trend as the heat of reduction (Table 1) over the entire range of temperature and pressure considered.

Carbonation of PuO_2 Surfaces - By plotting the surface energy of PuO_2 stoichiometric and oxygen-deficient surfaces (both bare and carbonated) as a function of temperature and partial pressure of CO_2 (Equation 6 to Equation 8), phase diagrams mapping the carbonation of PuO_2 surfaces can be drawn (Figure 5A-F). At a lower temperature, the surfaces of PuO_2 are all carbonated, whereas CO_2 desorbs at high temperature leaving the bare surfaces exposed. Figures 5G-H summarises the temperature of desorption of CO_2 from the surfaces, *i.e.* the highest temperature needed at specific conditions of CO_2 pressure for the CO_2 to leave the surface. CO_2 desorbs at lower temperatures on the {111}, followed by the {110} and the {100}.

On all surfaces the CO_2 desorbs at lower temperature on the stoichiometric (Figure 5G) compared to the oxygen-deficient (Figure 5H) surfaces, with differences in temperature between the two as low as 60 K and as high as 225 K (Figure 5I).

Adsorption experiments of CO_2 on $PuO_{2.00}$ powder have been conducted by Colmenares and Terada[17] and Stakebake[6] who both demonstrated that the oxide powder absorbed greater amounts of CO_2 at lower temperatures. The former study derived average heats of adsorption of 0.28 to 0.52 eV (30 to 90 °C) whereas the latter reported a heat of adsorption of 0.12 eV at -80 °C. The studies agree that physisorption dominates at low temperatures and that the higher temperature range values are indicative of some component of the gas chemisorbing. Stakebake and Dringman[18] studied the desorption of various gases from PuO_2 exposed to air and found the majority of mass loss (~90-95%) was below 700 °C with CO_2 being released up to 1000 °C but predominantly over the range 100-600 °C. Interestingly, this work identifies two maxima in the release data with two different samples: the first at 200 °C and 500 °C, and the second at 250-300 °C and 400 °C. This variation in the detection of CO_2 with temperature is indicative a range of desorbing species. Whether this detected CO_2 is the result of desorbing molecular CO_2 or the decomposition of carbonate or hydrogen carbonate species cannot be determined from the experimental data available at this time.

The trend in desorption temperatures in Figure 5G-H shows that CO_2 will desorb at lower temperatures from the {111} surface (the most stable surface and thus most likely the one expressed the most in experimental samples), although we predict that CO_2 is retained on the {100} surface at higher temperature. Although our models do not account for co-adsorption of CO_2 and H_2O, it is worth mentioning that previous study of Stakebake[66] (experimental) and of Tegner *et al.*[43] (computational) have measured and predicted water desorption temperatures on PuO_2 surfaces to be in the range of 373K-623 K depending on surface morphology. These water desorption temperatures are in the same range of our predicted CO_2 desorption temperatures, suggesting that residual water may be adsorbed to the surface when CO_2 is present. Some of the data shown by Stakebake and Dringman[18] shows that there may be a relationship between the desorption of H_2O and CO_2 over the 300-500 °C temperature range. The influence of water adsorption on the desorption of CO_2 will require further study and should constitute further work.

Morphology of PuO_2 nanoparticle - By calculating the Wulff construction as a function of temperature and pressure, the total surface area for all of the exposed surfaces of a construction can be derived. By taking the surface area of a particular surface and comparing that to the total exposed surface area, the percentage area for that surface can be derived for a particular temperature and pressure of CO_2. This is presented in Figure 6A-C. The phase diagrams refer to oxygen-deficient surfaces (either carbonated or bare) as for the

View Article Online
DOI: 10.1039/D0CP00021C

stoichiometric surfaces, the {111} surface dominates the phase diagrams at all conditions of temperature and pressure and therefore there is no need to visually depict this. On the oxygen-deficient surfaces (Figure 6) the {111} surface is still the most dominant (Figure 6A), the {110} and the {100} surfaces are both predicted to be present (Figure 6B and 6C respectively). This can be usefully compared to Lavalley's[70] analysis of surfaces on ThO_2 nanopowder where {111} and {110} (but also {211}) account for the majority of the surface whereas the {100} is seen in much lower proportions.

The percentage area phase diagram in Figure 6 can also be used to distinguish whether the surfaces are carbonated or bare by overlaying the temperatures of desorption of CO_2 in Figure 5H as a dotted line. At all conditions on the left of the dotted line in Figure 6, the surfaces are carbonated, but as T and P(CO_2) increases above the temperature of desorption of CO_2, the surfaces are bare. This allows the reader to quickly ascertain whether the nanoparticles are carbonated or not. For example, in Figure 6C, the {111} at low pressure and high temperature (the bottom right corner of the phase diagram) the surface is bare, but at high temperature and high pressure (the top left of the phase diagram) the surface is carbonated. So in both regions of the diagram the nanoparticle will be an octahedron, but in the former example, the surface will be bare, whereas it will be carbonated in the latter. By combining the percentage area of the different surfaces of PuO_2 in Figure 6, we can retrieve the nanoparticle morphology of PuO_2 using the Wulff construction.[47] Figure 7 displays the most relevant PuO_2 nanoparticle morphologies within the interval of pressure of CO_2 and temperature studied. Again, we added the temperature of desorption of CO_2 (Figure 5H) to mark the boundary between carbonated and bare surfaces. As temperature and pressure of CO_2 increase, there is a gradual loss of the {100} from the nanoparticle that changes from a truncated octahedral to an octahedral morphology. In this region, the {110} surface also appears in the morphology of the nanoparticle. This is due to the bare {111} becoming increasingly less stable compared to the carbonated {110} surface.

The literature around radiolytically driven corrosion acknowledges morphology effects, but remains more concerned with sample composition.[11] Here, we discuss our findings considering the morphology of actinide oxides within the literature. Castell[71] derived a truncated octahedral shape at high pressure and temperature for UO_2 voids using low voltage scanning electron microscopy. An octahedral morphology is generally predicted in computational studies too. Jomard and Bottin[72] using DFT + *U* (1k AFM ordering and no SOI), predicted an octahedral morphology for PuO_2 at atmospheric pressure and room temperature, which suggests that at low temperature the {111} surface dominates the morphology. This is consistent with modelling studies of other actinide oxides including UO_2 (interatomic potential[67] and DFT[23]) and ThO_2 (DFT + *U*[55]). It is clear that these computational analyses corroborate our findings where the {111} surface is the dominant one due to a lower surface energy, both with and without CO_2.

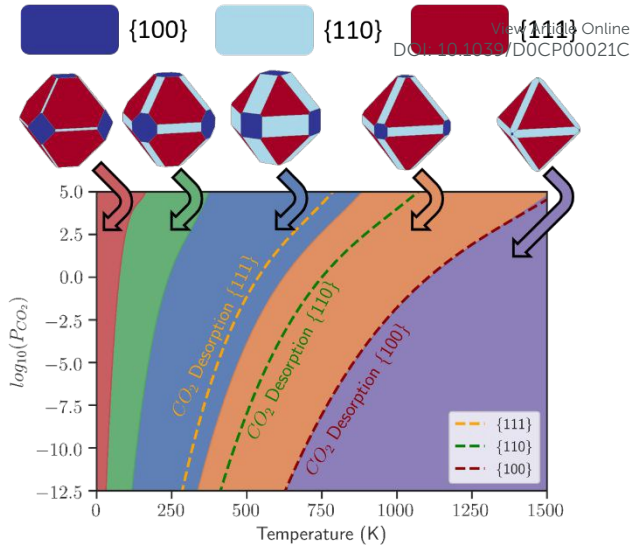

Figure 7 – A phase diagram to demonstrate the most stable Wulff constructions at particular regions of pressure and temperatures. The dotted lines denote the CO2 desorption.

Although the {110} surface has not been reported on PuO_2 nanoparticles as we do, the work of Castell[71] predicts the formation of the {110} surface as ridges of the {111} surface in UO_2 voids. These ridges disappear by transforming into {111} surfaces as the additional surface area created by the transformation compensates for the much lower surface energy of the {111} compare to the {110} surface. In our study, as we consider the adsorption of CO_2, we see that at the mid-range of partial pressure of CO_2 and temperature, there is a region where the {110} remains a stable surface stabilised by the adsorption of CO_2. This indicates that adsorbed CO_2, if present may deny the transformation of the {110} ridges into the most stable {111} surfaces.

Implications for Radiolytically Driven Dispersal

Radiolysis occurs at the interface of radioactive actinides and water. Whereas, the aim of this work is not to directly inform the reactions involved in radiolytic processes, we provide details on the surface composition of PuO_2. Any adsorbed species at the surface of the material inherently affects surface processes by increasing the availability of these species while reactive species are generated by radiolysis.[5] There is no general consensus on whether the presence of dissolved CO_2 either increases[9–12] or decreases[13,14] the rate of radiolytically driven environmental dispersal. It would seem logical, however, that since the rate of environmental dispersal is influenced by dissolved CO_2, then this might also be influenced by the adsorption/release of CO_2 from PuO_2 surfaces. Our data suggests that adsorbed CO_2 interacts strongly with the surfaces of PuO_2 (Table 2) and that relatively high temperatures are needed to fully desorb CO_2 from PuO_2 surfaces (Figure 5). The presence of adsorbed CO_2 has been suggested to aid the release of oxidised actinide species in the form of stable carbonate complexes.[73,74]

For radiation induced dissolution of UO_2, and thus presumably for PuO_2, it is suggested that the type of oxide and

surface morphology affect rate of dissolution.[11] To date, however, the effect of different surface morphologies on the rate of radiolysis is currently unexplored. We show that the strength of CO_2 adsorption strongly depends on surface morphology, which ultimately will affect the release of adsorbed CO_2 in solution. This, in turn may affect the extent of radiolytically driven dispersal depending if the presence of CO_2 increases[9–12] or decreases[13,14] the effect (in the case the PuO_2 acts as UO_2 does). We show that the strongest interaction between CO_2 and PuO_2 occurs on the {100} surface, followed by the {110} and {111} surfaces (Table 2). Therefore, control of the synthesis of PuO_2 nanoparticles will determine the availability of surface adsorbed CO_2.

Finally, we aid the prediction of the morphology of PuO_2 nanoparticles as a function of temperature and pressure (Figure 7). Although the Wulff construction only accounts for thermodynamic data, it is clear that there will be a thermodynamic driving force that may drive morphological changes during long term storage and this might change the rate of environmental dispersal under some conditions.

Conclusions

We have shown that it is possible to correlate the *ab initio* data at the molecular level with concepts of desorption temperatures, surface phase diagrams and nanoparticle morphology for PuO_2. We found that the oxygen-deficient surfaces of PuO_2 generally exhibit stronger adsorption of CO_2 compared to the stoichiometric surfaces. Morphologies of PuO_2 can differ over the range of temperatures and CO_2 pressure but remain of truncated octahedral shape. We have discussed our findings in the context of radiolytically driven reactions with groundwater and the presence of CO_2 (experimentally, it is uncertain whether and how dissolved CO_2 affects these reactions). In this study, we show that CO_2 adsorbed at the surfaces of PuO_2 will need to be taken into account as this CO_2 will be readily available to interfere with the radioactive soluble species. While we have focussed on the interaction of CO_2 with dry surfaces of PuO_2, there is room here for investigating other aspects of this work, notably the impact of water on CO_2 adsorption, and the extension of the modelling procedure to account for a greater complexity of molecular species. Finally, correlating our *ab initio* data to experimental data, such as those related to surface vibrational responses will provide essential insight into adsorbed species behaviour and conformation, and should constitute the object of further work.

Conflicts of Interest

There are no conflicts to declare.

Acknowledgement

We would like to acknowledge EPSRC (EP/R513234/1 and EP/R010366/1) and the EPSRC-funded CCP5 (EP/M022617/1) for funding. Computations were run on the Orion computing facility at the University of Huddersfield and the ARCHER UK National Supercomputing Service (http://www.archer.ac.uk) via our membership of the UK's HEC Materials Chemistry Consortium (HEC MCC) funded by EPSRC (EP/L000202, EP/R029431). To the extent that this paper relies on the contribution of Robert Harker then the copyright vests in the ©British Crown Copyright 2020/AWE. Data related to this research is available via the University of Huddersfield online repository.

Notes and References

Author Information

Corresponding Author
* Marco Molinari – m.molinari@hud.ac.uk
* Samuel Moxon – samuel.moxon@hud.ac.uk

ORCID

Samuel Moxon: 0000-0002-2972-5975
Adam R. Symington: 0000-0001-6059-497X
Joshua S. Tse: 0000-0002-1320-557X
James Dawson: 0000-0002-5669-0915
Joseph M. Flitcroft: 0000-0001-8373-0233
Stephen C. Parker: 0000-0003-3804-0975
David J. Cooke: 0000-0001-5996-7900
Robert M. Harker: 0000-0001-5108-8936
Marco Molinari: 0000-0001-7144-6075

References

1 Nuclear Decommissioning Authority, *Progress on Plutonium Consolidation, Storage and Disposition*, 2019.
2 A. Y. Romanchuk, T. V. Plakhova, A. V. Egorov, T. B. Egorova, P. V. Dorovatovskii, Y. V. Zubavichus, A. A. Shiryaev and S. N. Kalmykov, *Dalt. Trans.*, 2018, **47**, 11239–11244.
3 J. D. Farr, R. K. Schulze and M. P. Neu, *J. Nucl. Mater.*, 2004, **328**, 124–136.
4 Stockholm International Peace Research Institute, *SIPRI Yearbook 2019: Armaments, Disarmament and International Security*, Oxford University Press, 2019.
5 R. C. Ewing, *Nat. Mater.*, 2015, **14**, 252–257.
6 J. L. Stakebake, *J. Nucl. Mater.*, 1971, **38**, 241–259.
7 DOE, *Assessment of Safety Issues at Department of Energy Facilities Plutonium Storage*, 1994.
8 A. Traboulsi, J. Vandenborre, G. Blain, B. Humbert, J. Barbet and M. Fattahi, *J. Phys. Chem. C*, 2014, **118**, 1071–1080.
9 A. Kitamura and H. Takase, *J. Nucl. Sci. Technol.*, 2016, **53**, 1–18.
10 H. Christensen and S. Sunder, *Nucl. Technol.*, 2000, **131**, 102–123.
11 T. E. Eriksen, D. W. Shoesmith and M. Jonsson, *J. Nucl. Mater.*, 2012, 420, 409–423.
12 E. Ekeroth and M. Jonsson, *J. Nucl. Mater.*, 2003, **322**, 242–248.
13 J. De Pablo, I. Casas, F. Clarens, F. El Aamrani and M. Rovira, *MRS Proc.*, 2000, **663**, 409.
14 A. Barreiro Fidalgo, Y. Kumagai and M. Jonsson, *J. Coord.*

Chem., 2018, **71**, 1799–1807.
15 M. M. Hossain, E. Ekeroth and M. Jonsson, *J. Nucl. Mater.*, 2006, **358**, 202–208.
16 H. L. Yu, X. D. Deng, G. Li, X. C. Lai and D. Q. Meng, *Appl. Surf. Sci.*, 2014, **316**, 625–631.
17 C. A. Colmenares and K. Terada, *J. Nucl. Mater.*, 1975, **58**, 336–356.
18 J. L. Stakebake and M. R. Dringman, *Desorption from Plutonium Dioxide*, Golden, CO, 1968.
19 O. J. Wick, *Plutonium handbook: a guide to the technology*, Gordon and Breach, New York, 1967.
20 J. T. Pegg, X. Aparicio-Anglès, M. Storr and N. H. de Leeuw, *J. Nucl. Mater.*, 2017, **492**, 269–278.
21 J. T. Pegg, A. E. Shields, M. T. Storr, A. S. Wills, D. O. Scanlon and N. H. de Leeuw, *Phys. Chem. Chem. Phys.*, 2018, **20**, 20943–20951.
22 J. T. Pegg, A. E. Shields, M. T. Storr, D. O. Scanlon and N. H. de Leeuw, *J. Chem. Phys.*, 2019, **150**, 134701–134710.
23 J. T. Pegg, A. E. Shields, M. T. Storr, D. O. Scanlon and N. H. de Leeuw, *J. Phys. Chem. C*, 2019, **123**, 356–366.
24 G. Kresse and J. Furthmüller, *Phys. Rev. B*, 1996, **54**, 11169–11186.
25 J. Heyd, G. E. Scuseria and M. Ernzerhof, *J. Chem. Phys.*, 2003, **118**, 8207–8215.
26 J. Heyd, G. E. Scuseria and M. Ernzerhof, *J. Chem. Phys.*, 2006, **124**, 219906.
27 J. P. Perdew, A. Ruzsinszky, G. I. Csonka, O. A. Vydrov, G. E. Scuseria, L. A. Constantin, X. Zhou and K. Burke, *Phys. Rev. Lett.*, 2008, **100**, 136406.
28 P. Santini, R. Lémanski and P. Erdős, *Adv. Phys.*, 1999, **48**, 537–653.
29 J. C. Boettger and A. K. Ray, *Int. J. Quantum Chem.*, 2002, **90**, 1470–1477.
30 C. E. McNeilly, *J. Nucl. Mater.*, 1964, **11**, 53–58.
31 J. P. Perdew and A. Zunger, *Phys. Rev. B*, 1981, **23**, 5048–5079.
32 A. I. Liechtenstein, V. I. Anisimov and J. Zaanen, *Phys. Rev. B*, 1995, **52**, R5467–R5470.
33 S. L. Dudarev, G. A. Botton, S. Y. Savrasov, C. J. Humphreys and A. P. Sutton, *Phys. Rev. B*, 1998, **57**, 1505–1509.
34 H. Wang and K. Konashi, *J. Alloys Compd.*, 2012, **533**, 53–57.
35 R. C. Belin, P. J. Valenza, M. A. Reynaud and P. E. Raison, *J. Appl. Crystallogr.*, 2004, **37**, 1034–1037.
36 L. B. Asprby, F. H. Ellinger, S. Fried and W. H. Zachariasen, *J. Am. Chem. Soc.*, 1955, **77**, 1707–1708.
37 W. H. Zachariasen, *Acta Crystallogr.*, 1949, **2**, 388–390.
38 D. Taylor, *Trans. J. Br. Ceram. Soc.*, 1984, **83**, 32–37.
39 T. D. Chikalla, C. E. McNeilly and R. E. Skavdahl, *J. Nucl. Mater.*, 1964, **12**, 131–141.
40 G. W. Watson, E. T. Kelsey, N. H. de Leeuw, D. J. Harris and S. C. Parker, *J. Chem. Soc. Faraday Trans.*, 1996, **92**, 433.
41 Q. Sun, K. Reuter and M. Scheffler, *Phys. Rev. B*, 2003, **67**, 205424.
42 M. Molinari, S. C. Parker, D. C. Sayle and M. S. Islam, *J. Phys. Chem. C*, 2012, **116**, 7073–7082.
43 B. E. Tegner, M. Molinari, A. Kerridge, S. C. Parker and N. Kaltsoyannis, *J. Phys. Chem. C*, 2017, **121**, 1675–1682.
44 S. Kerisit, A. Marmier and S. C. Parker, *J. Phys. Chem. B*, 2005, **109**, 18211–18213.
45 A. R. Symington, M. Molinari, S. Moxon, J. M. Flitcroft, D. C. Sayle and S. C. Parker, *J. Phys. Chem. C*, 2020, **124**, 3577–3588.
46 M. W. Chase, *NIST-JANAF Thermochemical Tables, 4th Edition | NIST*, American Institute of Physics, 1998.
47 G. Wulff, *Zeitschrift für Krist. - Cryst. Mater.*, 1901, **34**, 449–530.
48 K. Momma, F. Izumi and IUCr, *J. Appl. Crystallogr.*, 2011, **44**, 1272–1276.
49 A. Symington, J. Tse, M. Molinari, A. Marmier and S. Parker, *J. Open Source Softw.*, 2019, **4**, 1210–1211.
50 R. Tran, Z. Xu, B. Radhakrishnan, D. Winston, W. Sun, K. A. Persson and S. P. Ong, *Sci. Data*, 2016, **3**, 160080.
51 Z. Rák, R. C. Ewing and U. Becker, *Surf. Sci.*, 2013, **608**, 180–187.
52 B. Sun, H. Liu, H. Song, G. Zhang, H. Zheng, X. Zhao and P. Zhang, *J. Nucl. Mater.*, 2012, **426**, 139–147.
53 C. Muggelberg, M. . Castell, G. A. . Briggs and D. . Goddard, *Appl. Surf. Sci.*, 1999, **142**, 124–128.
54 M. Nolan, S. Grigoleit, D. C. Sayle, S. C. Parker and G. W. Watson, *Surf. Sci.*, 2005, **576**, 217–229.
55 A. E. Shields, D. Santos-Carballal and N. H. de Leeuw, *J. Nucl. Mater.*, 2016, **473**, 99–111.
56 V. Alexandrov, T. Y. Shvareva, S. Hayun, M. Asta and A. Navrotsky, *J. Phys. Chem. Lett.*, 2011, **2**, 3130–3134.
57 R. Chatzimichail, S. Bebelis and P. Nikolopoulos, *J. Mater. Eng. Perform.*, 2016, **25**, 1691–1696.
58 E. N. Hodkin and M. G. Nicholas, *J. Nucl. Mater.*, 1977, **67**, 171–180.
59 J. P. W. Wellington, B. E. Tegner, J. Collard, A. Kerridge and N. Kaltsoyannis, *J. Phys. Chem. C*, 2018, **122**, 7149–7165.
60 M. Molinari, A. R. Symington, D. C. Sayle, T. S. Sakthivel, S. Seal and S. C. Parker, *ACS Appl. Bio Mater.*, 2019, **2**, 1098–1106.
61 C.-Y. Zhou, D. Wang and X.-Q. Gong, *Phys. Chem. Chem. Phys.*, 2019, **21**, 19987–19994.
62 T. X. T. Sayle, M. Molinari, S. Das, U. M. Bhatta, G. Möbus, S. C. Parker, S. Seal and D. C. Sayle, *Nanoscale*, 2013, **5**, 6063–6073.
63 P. M. Albrecht, D. Jiang and D. R. Mullins, *J. Phys. Chem. C*, 2014, **118**, 9042–9050.
64 D. R. Mullins, *Surf. Sci. Rep.*, 2015, 70, 42–85.
65 U. Castanet, C. Feral-Martin, A. Demourgues, R. L. Neale, D. C. Sayle, F. Caddeo, J. M. Flitcroft, R. Caygill, B. J. Pointon, M. Molinari and J. Majimel, *ACS Appl. Mater. Interfaces*, 2019, **11**, 11384–11390.
66 J. L. Stakebake, *J. Phys. Chem.*, 1973, **77**, 581–586.
67 A. H. H. Tan, R. W. Grimes and S. Owens, *J. Nucl. Mater.*, 2005, **344**, 13–16.
68 J. M. Haschke and T. E. Ricketts, *J. Alloys Compd.*, 1997, **252**, 148–156.
69 C. Zhang, Y. Yang and P. Zhang, *Sci. China Physics, Mech. Astron.*, 2019, **62**, 107002–107007.
70 X. Montagne, J. Lynch, E. Freund, J. Lamotte and J. C.

View Article Online
DOI: 10.1039/D0CP00021C

Lavalley, *J. Chem. Soc. Faraday Trans. 1 Phys. Chem. Condens. Phases*, 1987, **83**, 1417–1425.
71 M. R. Castell, *Phys. Rev. B*, 2003, **68**, 235411.
72 G. Jomard and F. Bottin, *Phys. Rev. B*, 2011, **84**, 195469.
73 S. Kerisit and C. Liu, *Environ. Sci. Technol.*, 2012, **46**, 1632–1640.
74 S. Stroes-Gascoyne and J. S. Betteridge, *MRS Proc.*, 2004, **824**, CC9.9.